Chemistry Europe
European Chemical Societies Publishing

WILEY VCH

Excellence in Chemistry Research

Announcing our new flagship journal

- Gold Open Access
- Publishing charges waived
- Preprints welcome
- Edited by active scientists

Meet the Editors of *ChemistryEurope*

Luisa De Cola
Università degli Studi di Milano Statale, Italy

Ive Hermans
University of Wisconsin-Madison, USA

Ken Tanaka
Tokyo Institute of Technology, Japan

Chemistry–A European Journal
Research Article
doi.org/10.1002/chem.202301315
Chemistry Europe
European Chemical Societies Publishing
www.chemeurj.org

Molecular and Crystal Structure, Spectroscopy, and Photochemistry of a Dispiro Compound Bearing the Tetraoxane Pharmacophore

Patrícia S. M. Amado,[a, b] Susy Lopes,[c] Elisa M. Brás,[c] José A. Paixão,[d] Ma-aya Takano,[e, f] Manabu Abe,[e, f] Rui Fausto,*[c, g] and Maria L. S. Cristiano*[a, b]

The molecular structure and photochemistry of dispiro[cyclohexane-1,3′-[1,2,4,5]tetraoxane-6′,2′′-tricyclo[3.3.1.1^{3,7}]decan]-4-one (**TX**), an antiparasitic 1,2,4,5-tetraoxane was investigated using matrix isolation IR and EPR spectroscopies, together with quantum chemical calculations undertaken at the DFT(B3LYP)/6-311++G(3df,3pd) level of theory, with and without Grimme's dispersion correction. Photolysis of the matrix-isolated TX, induced by in situ broadband ($\lambda > 235$ nm) or narrowband (λ in the range 220–263 nm) irradiation, led to new bands in the infrared spectrum that could be ascribed to two distinct photoproducts, oxepane-2,5-dione, and 4-oxohomoadamantan-5-one. Our studies show that these photoproducts result from initial photoinduced cleavage of an O–O bond, with the formation of an oxygen-centered diradical that regioselectivity rearranges to a more stable (secondary carbon-centered)/(oxygen-centered) diradical, yielding the final products. Formation of the diradical species was confirmed by EPR measurements, upon photolysis of the compound at $\lambda = 266$ nm, in acetonitrile ice ($T = 10$–80 K). Single-crystal X-ray diffraction (XRD) studies demonstrated that the **TX** molecule adopts nearly the same conformation in the crystal and matrix-isolation conditions, revealing that the intermolecular interactions in the **TX** crystal are weak. This result is in keeping with observed similarities between the infrared spectrum of the crystalline material and that of matrix-isolated **TX**. The detailed structural, vibrational, and photochemical data reported here appear relevant to the practical uses of **TX** in medicinal chemistry, considering its efficient and broad parasiticidal properties.

[a] *Dr. P. S. M. Amado, Prof. Dr. M. L. S. Cristiano*
Center of Marine Sciences, CCMAR, Gambelas Campus
University of Algarve
UAlg, 8005-139 Faro (Portugal)
E-mail: mcristi@ualg.pt

[b] *Dr. P. S. M. Amado, Prof. Dr. M. L. S. Cristiano*
Department of Chemistry and Pharmacy
Faculty of Sciences and Technology, Gambelas Campus
University of Algarve
UAlg, 8005-139 Faro (Portugal)

[c] *Dr. S. Lopes, Dr. E. M. Brás, Prof. Dr. R. Fausto*
CQC-IMS, Department of Chemistry
University of Coimbra
3004-535 Coimbra (Portugal)
E-mail: rfausto@ci.uc.pt

[d] *Prof. Dr. J. A. Paixão*
CFisUC, Department of Physics
University of Coimbra
3004-516 Coimbra (Portugal)

[e] *Dr. M.-a. Takano, Prof. Dr. M. Abe*
Department of Chemistry
Graduate School of Advanced Science and Engineering
Hiroshima University
Higashi-Hiroshima, Hiroshima, 739-8526 (Japan)

[f] *Dr. M.-a. Takano, Prof. Dr. M. Abe*
International Institute for Sustainability with Knotted Chiral Meta Matter (SKCM^2)
Higashi-Hiroshima, Hiroshima, 739-0046 (Japan)

[g] *Prof. Dr. R. Fausto*
Faculty of Sciences and Letters, Department of Physics
Istanbul Kultur University
Ataköy Campus, Bakirköy 34156, Istanbul (Turkey)

Supporting information for this article is available on the WWW under https://doi.org/10.1002/chem.202301315

Introduction

Organic peroxides are found in various natural products as biologically active compounds and take part in chemical reactions as intermediates.[1]

Among organic peroxides, five- and six-membered 1,2,4-trioxolanes and 1,2,4,5-tetraoxanes have gained significant applicability in medicinal chemistry due to their potential for treating malaria and other diseases.[2–5] The interest in cyclic organic peroxides is mainly due to the 1,2,4-trioxane pharmacophoric moiety in artemisinin (ART). This natural product integrates the arsenal of frontline antimalarial drugs, together with some of its semi-synthetic derivatives.[6–10]

The mechanism of bioactivation and action of related endoperoxide-based drugs has been discussed thoroughly.[9,11–13]

Bioactivation is thought to require iron(II)-induced reductive cleavage of the peroxide bond to form oxygen-centered radicals, followed by rearrangement to generate carbon-centered radicals that act through the alkylation of parasites' biological targets. While 1,2,4-trioxolanes generate only secondary carbon-centered radical species, it has been reported that 1,2,4,5-tetraoxanes can generate both primary and secondary carbon-centered radical species from Fe(II) reaction.[12] Interestingly, 1,2,4,5-tetraoxanes are remarkably stable compared to their trioxolane counterparts. This superior thermodynamic stability observed in 1,2,4,5-tetraoxanes was investigated by Gomes et al.[14] through theoretical calculations based on

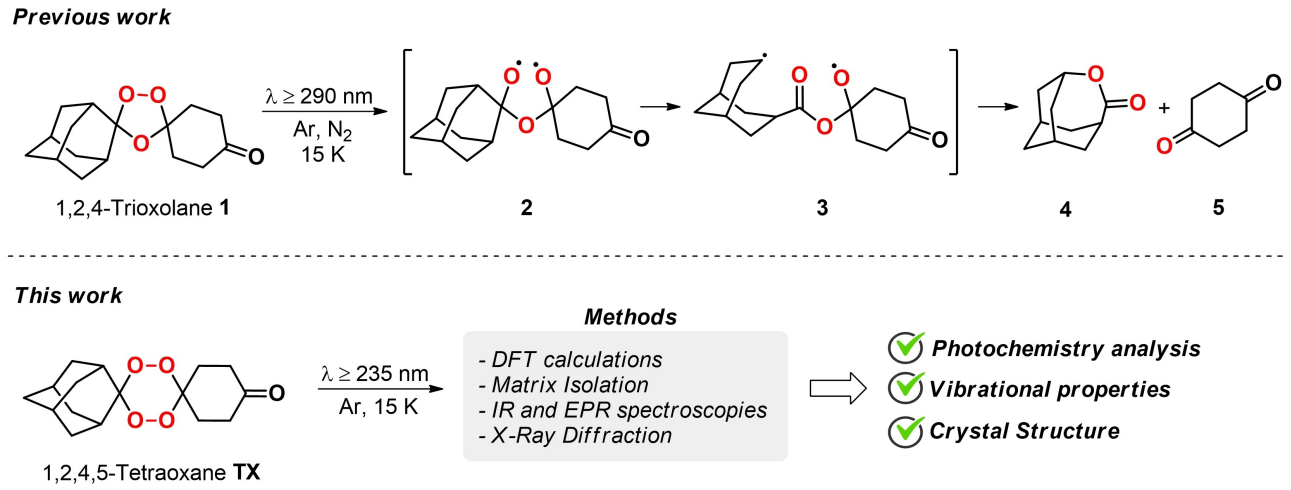

Scheme 1. Previous work[17] with adamantane-2-spiro-3′-8′-oxo-1′,2′,4′-trioxaspiro[4,5]decane **1** and the dispiro[cyclohexane-1,3′-[1,2,4,5]tetraoxane-6′,2″-tricyclo[3.3.1.1^{3,7}]decan]-4-one (**TX**) studied in the present work.

stereoelectronic analysis, the results ascribe the enhanced stability to the stereoelectronic double anomeric effect, stabilizing the six-membered ring system.[14–16]

In 2020, we demonstrated that irradiation ($\lambda \geq 290$ nm) of the matrix isolated adamantane-2-spiro-3′-8′-oxo-1′,2′,4′-trioxaspiro[4,5]decane **1** (Scheme 1),[17] a well-known ozonide with efficient and broad antiparasitic activity,[18–20] affords exclusively 4-oxahomoadamantan-5-one **4** and 1,4-cyclohexanedione **5**. These results suggested that the reaction proceeds via a dioxygen-centered diradical intermediate, formed upon homolytic cleavage of the labile peroxide bond, which regioselectivity isomerizes to the more stable secondary (carbon-centered)/(oxygen-centered) diradical. In situ EPR measurements during the photolysis of **1** deposited in a MeTHF-matrix led to the detection of signals corresponding to two triplet species, one of which was short-lived while the other proved to be persistent at 10 K. These observations strongly supported the proposed mechanism for the photogeneration of **4** and **5**, which involves intramolecular rearrangement of the intermediate diradical species **2** to afford the triplet diradical **3**.

As a continuation of the previous work, we investigated the structure and matrix photochemistry of dispiro[cyclohexane-1,3′-[1,2,4,5]tetraoxane-6′,2″-tricyclo[3.3.1.1^{3,7}]decan]-4-one (**TX**; see Scheme 1), a tetraoxane analogue of the 1,2,4-trioxolane **1**. Our studies involved matrix isolation infrared (IR) and electron paramagnetic resonance (EPR) spectroscopies, combined with B3LYP/6-311++G(3df,3dp) calculations, which were used to obtain structural information on **TX** and the photoproduced species, and their spectroscopic properties, to support the experimentally obtained IR spectroscopy data analysis. Subsequently, the EPR spectroscopy searched for the diradicals generated under UV-photolysis of the compound isolated in a low-temperature acetonitrile matrix. The structure of 1,2,4,5-tetraoxane **TX** was also investigated in the crystalline phase, using X-ray crystallography and IR spectroscopy.

Results and Discussion

Predicted conformers of TX – structures and relative energies

The **TX** structure comprehends three moieties: an adamantane fragment, a *p*-cyclohexanone ring, and the 1,2,4,5-tetraoxane ring that connects the adamantane and *p*-cyclohexanone fragments, generating the dispiro structure. The adamantane group is a conformationally rigid structure, while both the cyclohexanone and tetraoxane rings can exist in different conformations. The performed search on the potential energy surface of **TX** revealed the existence of five different conformers of the compound, where the tetraoxane and cyclohexanone rings exhibit either a chair (**C**) or a twisted-boat (**TB**) arrangement. These conformers are depicted in Figure 1, together with their DFT(B3LYP)/6–311++G(3df,3pd) calculated relative zero-point-corrected relative energies. The

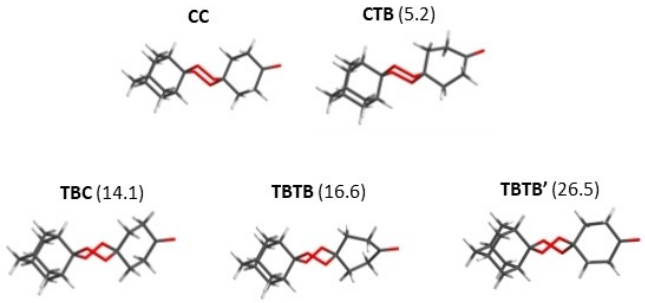

Figure 1. Conformers of TX, as predicted by the performed DFT(B3LYP)/6-311++G(3df,3pd) calculations. The numbers in parentheses are the relative zero-point-corrected energies (in kJ mol^{-1}) of the different conformers (relative to the most stable form, **CC**). **C**: Chair; **TB**: twisted-boat; in the conformers designation, the first letter(s) refers to the conformation of the tetraoxane ring, while the second letter(s) refers to the conformation of the cyclohexanone ring. Zero-point corrected calculated relative energies obtained with consideration of Grimme's three-body term dispersion correction D3 and Becke-Johnson damping are 5.9, 17.6, 20.5 and 30.7 kJ mol^{-1}, respectively for **CTB**, **TBC**, **TBTB** and **TBTB′**.

optimized geometries (Cartesian coordinates) of the five conformers are provided in the Supporting Information (Table S1). Inclusion of Grimme's three-body term dispersion correction D3 and Becke-Johnson (BJ) damping was found only to slightly change the relative energies of the conformers, leading to a small additional stabilization of the most stable conformer (see caption of Figure 1).

According to calculations, the most stable conformer of **TX** has both tetraoxane and cyclohexanone rings in the chair conformation (**CC**). The second conformer in the increasing order of energy, **CTB**, is 5.2 kJ mol^{-1} higher in energy (zero-point-corrected energy) than **CC**. In this conformer, the tetraoxane ring is in the chair conformation (like in **CC**), but the cyclohexanone ring assumes a twisted-boat conformation. Very interestingly, the increase in energy upon changing the conformation of the cyclohexanone ring from chair to twisted-boat is considerably smaller than when it is the tetraoxane ring to change its conformation from chair to twisted boat. In this latter case, the increase of energy is *ca.* 3 times larger (keeping the conformation of the cyclohexanone ring in the chair arrangement, i.e., in going from **CC** to **TBC**, which is higher in energy than **CC** by 14.1 kJ mol^{-1}). The **TBTB** and **TBTB'** conformers, where both tetraoxane and cyclohexanone rings assume a twisted-boat conformation, are 16.6 and 26.5 kJ mol^{-1} higher in energy than the most stable conformer (**CC**), respectively. The abundances of conformers **CC** and **CTB** in the gas-phase equilibrium at the sublimation temperature used to prepare the argon matrices of the studied compound (363 K), estimated taking into account their predicted relative energies and assuming a Boltzmann distribution, are 89% and 11%, respectively, the populations of the remaining conformers being negligible (< 0.5% in total).

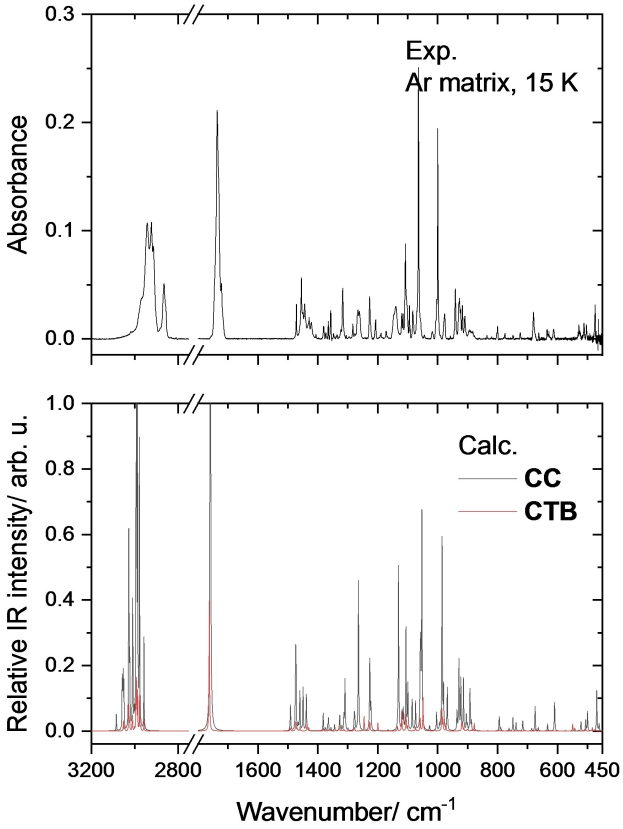

Figure 2. *Top*: infrared spectrum of **TX** isolated in an argon matrix (15 K); *bottom*: DFT(B3LYP)/6-311++G(3df,3pd) calculated infrared spectra (wavenumbers scaled by 0.983) of conformers **CC** and **CTB** of **TX** with intensities multiplied by their gas-phase equilibrium at 363 K predicted populations (89% **CC**; 11% **CTB**).

Infrared spectra of TX isolated in an argon matrix (15 K)

The infrared spectrum of **TX** monomers isolated in an argon matrix (15 K) is presented in Figure 2, together with the simulated spectra obtained at the DFT(B3LYP)/6-311++G(3df,3pd) level, for conformers **CC** and **CTB**, multiplied by their predicted populations in the gas-phase at the temperature used to sublimate the compound during the matrix deposition. Both conformers belong to the C_1 symmetry point group, with 123 fundamental vibrations, all of them expected to be infrared active. The full calculated vibrational data for the two conformers is provided in the Supporting Information, Table S2.

As seen in the figure, the calculated spectrum of conformer **CC** reproduces very well the observed spectrum. On the other hand, conformer **CTB** does not seem to be present in the matrix. While there are a few bands that could be ascribed to this conformer (e.g., those at 1406.0, 1191.0 and 775.0 cm^{-1}, which appear at relatively close frequencies to those calculated for the **CTB** form at 1430.6, 1200.1 and 770.9 cm^{-1}), the intense **CTB** predicted bands at 1245.9, 549.9 and 542.7 cm^{-1} that should be observed experimentally if **CTB** were present in the matrix since, according to the calculations, they are not coincident with any band from the **CC** conformer, have no experimental counterparts. In addition, the deposition of matrices using different sublimation temperatures gave rise to identical spectra, and annealing of the deposited matrices to higher temperatures did not lead to any spectral change consistent with the putative conversion of conformer **CTB** into **CC**, both results also supporting the sole existence of conformer **CC** in the as-deposited matrices. Hence, though the presence in the as-deposited matrix of conformer **CTB** cannot be firmly excluded, its conversion to the most stable **CC** form during matrix deposition appears very much probable. In turn, this implies a low energy barrier separating these two species. In agreement with this hypothesis is the low energy barrier reported for the conversion between the twisted-boat and chair conformation in cyclohexanone itself, found to be of only *ca.* 9 kJ mol^{-1}.[21,22] Such a barrier is considerably lower than that in cyclohexane (> 20 kJ mol^{-1}[23]), and it is within the energy range of barriers that can be expected to be overcome during matrix deposition at the used substrate temperature (15 K).[24]

The assignment of the bands observed in the experimental IR spectrum of matrix-isolated **TX** is given in Table 1. In this table, alternative assignments to the **CC** conformer are given for the few bands mentioned above that *a priori* could also be

Table 1. Assignment of the infrared spectrum of **TX** isolated in an argon matrix (15 K) and DFT(B3LYP)/6-311++G(3df,3pd) calculated infrared data for conformer **CC**.[a]

Exp. (Ar matrix)	Calculated (CC)		Approximate description	Exp. (Ar matrix)	Calculated (CC)		Approximate description
	ν	I^{IR}			ν	I^{IR}	
n.obs.	3085.0	4.3	νCH_2 as *m* chx	**1228.0**	1227.5	10.6	$twCH_2$ ad
3020.0	3058.6	11.6	νCH_2 as *o* chx	**1224.5**	1226.5	13.7	$twCH_2$ *m*, *o* chx
	3056.1	11.6	νCH_2 as *o* chx	**1208.0**	1222.8	6.6	νCC chx
	3053.5	13.5	νCH prox ad	**1172.0**	1165.5	0.3	$twCH_2$ ad
	3050.6	11.9	νCH_2 as *m* chx	**1147.0/1140.0 FR**[c]	1131.1	44.8	$\nu C_\alpha C$ chx
2969.5	3028.7	27.2	νCH_2 as ad	**1120.0**	1118.6	5.0	δCH ad
	3027.6	41.5	νCH_2 as ad	**1116.0**	1116.0	0.05	δCH ad
	3024.4	13.3	νCH_2 as ad		1115.0	5.4	δCH ad
	3023.0	11.9	νCH_2 as ad	**1108.0**	1106.2	27.8	γCH_2 ad
	3010.6	31.5	νCH prox ad		1104.8	1.1	γCH_2 ad
	3008.6	17.0	νCH_2s *m* chx	**1103.0**	1099.7	13.2	νCC chx
	3002.8	3.8	νCH_2s *m* chx	**1094.0**	1085.4	8.4	γCH_2 ad
2943.0	2995.0	56.2	νCH_2 as term ad	**1083.0**	1074.1	7.8	νCC ad
2924.0	2992.4	110.4	νCH all-in-phase ad; νCH_2s ad	**1070.0**	1058.6	16.3	νCC ad"; νCO s (ad-side)
2915.0	2987.8	84.9	νCH ad	**1064.0**	1057.0	18.3	νCC ad
	2984.1	8.8	νCH_2s *o* chx	**1058.0**	1053.1	59.0	νCO s (chx-side)
	2978.5	76.0	νCH_2s ad	**1045.0**	1027.4	1.3	νCC ad
	2978.0	1.4	νCH_2s *o* chx	**1019.0**	1004.0	4.9	νCC chx
	2975.4	0.2	νCH_2s ad	**1006.5**	994.4	1.6	νCC ad
	2974.7	0.7	νCH_2s ad	**1000.0**	985.7	53.5	νCO s (ad-side)
	2972.6	0.1	νCH_2s ad	**1003.5**	980.5	11.2	νCO as (ad-side); νCC ad
2865.5	2957.9	25.1	νCH_2s term ad	**977.0**	968.1	11.8	νCC chx
1736.0	1759.1	286.8	νC=O	**941.0**	935.9	5.2	νOO s
1471.5	1491.6	7.0	δCH_2 ad	**928.0/927.0 FR**[d]	929.4	19.1	νCC ad
1455.0	1475.4	4.2	δCH_2*m* chx	**924.0**	922.8	14.3	γCH_2 *m* chx
	1474.2	12.6	δCH_2 ad	**918.0**	914.1	14.1	γCH_2 *m* chx
	1473.4	14.0	δCH_2 ad	**910.0**	904.7	4.4	νCO as (chx-side); νCC chx
1450.0	1465.6	1.5	δCH_2 term ad		901.2	1.7	νCC ad
1444.0	1460.3	10.4	δCH_2*m* chx	**895.0/891.0**[e]	892.2	11.9	γCH_2 *o* chx
	1460.0	0.9	δCH_2 ad	**887.0/882.0**[f]	887.5	2.5	γCH_2 term ad
1429.0	1449.6	11.7	δCH_2 *o* chx	**880.0**	880.3	0.02	γCH_2 ad
1422.0	1438.6	9.9	δCH_2 *o* chx	**877.0**	873.6	0.3	νOO as
1381.0	1382.3	5.0	δCH ad	**861.0**	859.4	0.03	νCC ad
1374.0	1374.4	0.8	δCH ad	**834.0**	833.2	0.1	νCC ad
1365.0	1366.9	1.1	wCH_2 ad	**800.5**	794.7	4.1	νCC chx
	1364.8	3.4	wCH_2*m*, *o* chx	**803.0**	789.4	0.9	νCC ad
	1362.0	0.04	δCH ad	**775.0**	762.0	0.7	νCC ad
1357.0	1356.6	0.9	wCH_2 ad	**749.0**	749.1	3.7	γC=O
1345.0	1344.5	1.7	wCH_2*m*, *o* chx	**746.0**	738.7	2.3	γCH_2 *o* chx
1338.5	1335.5	0.03	wCH_2 ad	**725.0**	716.4	2.8	νCC chx
	1334.6	0.03	wCH_2 ad	**680.5**	686.7	0.7	δCC chx
1335.0	1327.2	4.4	wCH_2*m*, *o* chx		675.2	6.9	δCC ad
1331.0	1319.9	1.2	δCH ad	**662.0/660.1**[g]	664.5	0.9	δCC ad
1323.0	1313.3	4.2	wCH_2 ad	**634.5**	633.5	1.9	δCC ad
1317.0	1309.5	13.8	$twCH_2$*m*, *o* chx	**613.0**	610.1	7.8	δCC chx
1306.0	1304.7	0.1	$twCH_2$ ad	**549.0**	546.7	0.2	δtox

Table 1. continued

Exp. (Ar matrix)	Calculated (CC)		Approximate description	Exp. (Ar matrix)	Calculated (CC)		Approximate description
	ν	I^{IR}			ν	I^{IR}	
	1299.6	0.6	twCH_2 ad	**529.0**	530.9	0.2	τtox
1283.0	1278.6	4.3	twCH_2 ad		522.0	2.6	τtox
1276.5	1276.7	3.2	δCH ad	**512.0**	506.2	3.0	δC=O
1266.0/1262.0 FR[b]	1264.7	41.7	twCH_2*m* chx; wCH_2 *o* chx	**504.0**	500.0	5.3	δ skeletal
	1261.2	0.3	νCC ad	**475.0**	469.3	11.4	δ skeletal
	1254.0	0.1	twCH_2 term ad	**464.0**	461.6	1.9	δ skeletal

[a] Calculated wavenumbers (ν) in cm^{-1}, were scaled by 0.983. Infrared intensities (I^{IR}) in km mol^{-1}. FR, Fermi resonance; n.obs., not observed; ν, stretching; δ, bending; w, wagging; tw, twisting; γ, rocking; τ, torsion; ad, adamantane moiety; chx, cyclohexanone ring; tox, tetraoxane ring; *m*, *meta*; *o*, *ortho*; as, anti-symmetric; s, symmetric; prox, proximal; term, terminal. [b] Fermi resonance with 1058.0 + 205.3 (calc) cm^{-1}; [c] Fermi resonance with 1000.0 + 151.0 (calc) cm^{-1}; [d] Fermi resonance with 2 × 464.0 cm^{-1}; [e] Fermi resonance with 464.0 + 431.0 (calc) cm^{-1}; [f] Fermi resonance with 464.0 + 424.3 (calc) cm^{-1}; [g] Fermi resonance with 2 × 326.5 (calc) cm^{-1}. Additional bands due to combination tones are observed at 627.0 ≈ 360.0 + 270.1 (calc.) cm^{-1}, 1191.0 = 1000 + 205 (calc) cm^{-1}, 1406.0 = 725.0 + 680.5 cm^{-1} and 1722.0 = 1058.0 + 662.0 cm^{-1}.

considered as originated in conformer **CTB**. The assignments were made straightforwardly, given the good reproducibility of the experimental data by the calculated spectrum of conformer **CC**, which only be discussed further for a few cases.

The first note to be made relates to the CH stretching modes, which are predicted to be considerably intense and were also observed as high-intensity bands. Usually, for matrix-isolated molecules the intensity of the CH stretching mode is much lower than the predicted one.[25] However, this is not the case in **TX**, particularly for the vibrations of the adamantane moiety (see Table 1), which then appears as an exception to the general rule. As it could be anticipated, the most intense band in the spectrum is due to the stretching of the C=O bond (observed at 1736.0 cm^{-1}; calculated: 1759.1 cm^{-1}), while the in-plane-bending and out-of-plane-rocking of the carbonyl are observed at 512.0 and 749.0 cm^{-1}, respectively, in good agreement with the calculated data (506.2 and 749.1 cm^{-1}). The stretching modes of the O–O peroxide bonds are observed at 941.0 and 877.0 cm^{-1} (symmetric and anti-symmetric vibrations, respectively. These bands are weak and appear at close frequencies to those predicted by the calculations (935.9 and 873.6 cm^{-1}, respectively). On the contrary, the C–O stretching vibrations are associated with intense bands (symmetric modes) or medium intensity bands (anti-symmetric modes). The symmetric C–O stretching of the adamantane side of the molecule is observed at 1000.0 cm^{-1} (predicted, 985.7 cm^{-1}), and that of the cyclohexanone side appears at 1058.0 cm^{-1} (predicted 1053.1 cm^{-1}), while the corresponding anti-symmetric modes are observed at 1003.5 and 910 cm^{-1} (predicted at 980.5 and 904.7 cm^{-1}). The methylene and methine deformation bands, as well as the CC stretching modes, are observed in the usual ranges and in good agreement with the calculations (see Table 1). Most of these modes are predicted to correspond to extensively delocalized vibrations throughout the various CH_2 or CH groups of a given moiety (adamantane or cyclohexanone), though there are exceptions to this general rule, which are duly indicated in Table 1. Most of these exceptions correspond to vibrations either of the CH groups of the adamantane fragment that are located closer to the tetraoxane ring (designated in Table 1 as "proximal") or of the CH_2 group of the adamantane moiety that stays more distant from this ring (designated as "terminal" in the table).

The calculations predict two particular vibrations to give rise to intense bands (> 40 km mol^{-1}), and these assignments also deserve further comments. These vibrations are predicted at 1264.7 and 1131.1 cm^{-1} and correspond, respectively, to a mixed twisting vibration of the *meta* CH_2 groups (relatively to the carbonyl) and wagging vibration of the *ortho* CH_2 groups, in the cyclohexanone ring and to the symmetric C_α–C stretching vibration (where α designates the carbon atoms in position-α to the carbonyl group) of the same ring. Experimentally, these vibrations give rise to bands that are observed as clearly distinguishable Fermi resonance doublets at 1266.0/1262.0 and 1147.0/1140.0 cm^{-1}, respectively (see Figure 2). The vibrations that most probably participate in the Fermi resonance interactions with these two fundamental modes are the combination tones whose fundamentals give rise to the intense bands at 1058.0 and 1000.0 cm^{-1} (symmetric C–O stretching modes), respectively, with the vibrations whose fundamentals are predicted at 205.3 and 151.0 cm^{-1} (outside the experimentally accessible spectral region to our instrumentation) and that are ascribable to the two C_α–C torsional vibrations of the cyclohexanone ring.

A final note shall be made here regarding the interesting observation that the IR spectrum of **TX** isolated in an argon matrix does not show evidence of matrix-site splitting, which is a common phenomenon in the spectra of matrix-isolated molecules, in particular for heterocyclic molecules,[26,27] and that is a consequence of trapping of molecules in different matrix sites (different matrix sites create different intermolecular potentials that may affect the intramolecular vibrational potential of the matrix-isolated molecules differently, originating splitting of the bands given the rise by the modes more affected by this interaction). The absence of matrix-site splitting indicates that the **TX** molecules probably occupy a single site in the argon matrix (or, alternatively, sites that are spectroscopically equivalent).

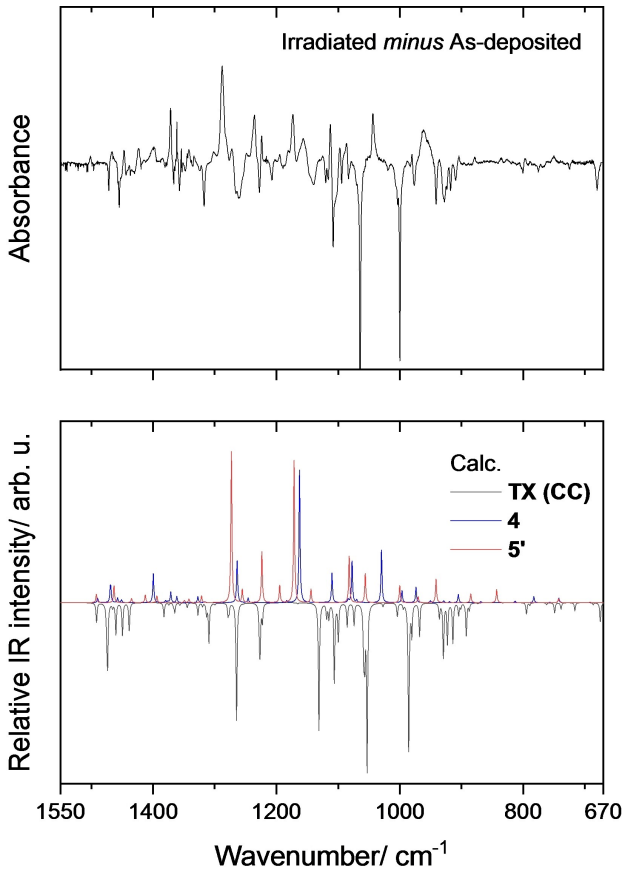

Figure 3. *Top*: infrared difference spectrum obtained by subtracting the spectrum of the as-deposited matrix of **TX** from that recorded after irradiation ($\lambda > 235$ nm) for 60 min of **TX** isolated in an argon matrix (15 K); *bottom*: DFT(B3LYP)/6-311++G(3df,3pd) calculated infrared spectra (wavenumbers scaled by 0.983) of TX (conformer **CC**; bands pointing down) and photoproducts **4** (4-oxohomoadamantan-5-one) and **5′** (oxepane-2,5-dione).

Broadband UV ($\lambda > 235$ nm) and narrowband UV (λ in the 220–263 nm range) irradiation of TX isolated in an Ar matrix (15 K)

Broadband UV ($\lambda > 235$ nm) and narrowband UV ($\lambda = 220$, 230, 250, 263 nm) irradiations of **TX** isolated in an argon matrix were undertaken in order to investigate the photochemistry of the compound under the used experimental conditions. Since the results obtained with the two types of irradiation, were the same in practical terms, we will focus on the data obtained upon broadband irradiation, which resulted to be more efficient.

Upon broadband UV ($\lambda > 235$ nm) irradiation of the matrix-isolated **TX**, the changes in the IR spectra of the matrix were already noticeable after a few minutes of irradiation, with the bands due to **TX** reducing in intensity and new bands, due to photoproduced species, starting to emerge. Figure 3 shows the IR difference spectrum obtained by subtracting the spectrum of the as-deposited matrix from that recorded after irradiation for 60 min.

As for other compounds bearing peroxide bonds, homolytic cleavage of the O–O bonds in **TX** appears as the most probable primary photoreaction.[17,28,29] An analogous photochemistry to the one we observed before in the case of the matrix isolated dispiro-1,2,4-trioxolane **1** (see Scheme 2)[17] appeared very much plausible also for **TX**, considering the structural similarity of the two compounds. Detailed analysis of the IR spectroscopic data collected during the photolysis of **TX** confirmed that the final major observed photoproducts were 4-oxohomoadamantan-5-one and oxepane-2,5-dione (**4** and **5′** in Scheme 2), which correspond to the expected products from a mechanism identical to that previously reported for compound **1**.[17] After the photocleavage of an O–O bond, an oxygen-centered diradical is formed (**2′**), which regioselectively rearranges to the more stable (secondary carbon-centered)/(oxygen-centered) diradical species **3′**, which then reorganizes to the final products **4** and **5′**. The regioselectivity of the rearrangement followed by the oxygen-centered diradical is confirmed by the absence of the

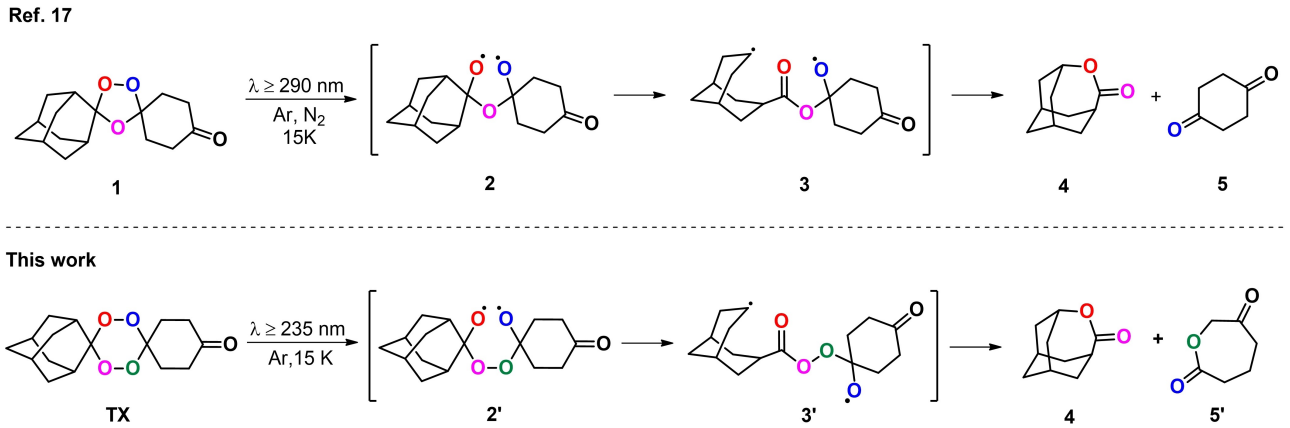

Scheme 2. Mechanisms proposed for the observed UV-induced photolysis of matrix-isolated adamantane-2-spiro-3′-8′-oxo-1′,2′,4′-trioxaspiro[4,5]decane **1**, previously reported in Ref. [17], and for the presently investigated UV-induced photolysis of **TX**, under similar experimental conditions.

alternative products (2-adamantanone and 1,2-dioxocane-3,6-dione; Figure S6 in the Supporting Information) in the photolysed matrix and is justified by the expected greater stability of the (secondary carbon-centered)/(oxygen-centered) diradical species **3′**, in comparison with the putative alternative (primary carbon-centered)/(oxygen-centered) diradical.

The identification of the photoproducts was made based on the comparison of the experimentally obtained spectral data with calculated IR spectra for the expected products of photolysis of **TX** and also taking into account the results of our previous investigation on the dispiro-1,2,4-trioxolane **1**.[17]

As shown in Figure 3, the bands emerging upon photolysis of **TX** are well-fitted by the combined spectra calculated for oxepane-2,5-dione and 4-oxohomoadamantan-5-one. The identification of oxepane-2,5-dione was unequivocal based on the excellent agreement between the frequencies of a set of new bands observed in the photolysed Ar matrix of **TX** and the theoretically simulated spectrum of the compound. Most of the predicted intense bands for this compound were observed in the spectra of the photolysed matrix. The only three medium intensity bands that were not detected (calculated at 1255.3, 1056.0, and 1000.2 cm^{-1}) have predicted frequencies very close to intense bands of **TX** (1266.0/1262.0 cm^{-1}, and 1003.5 and 1000 cm^{-1}, respectively). The results are shown in Table 2, while the full calculated spectrum of oxepane-2,5-dione is provided in the Supporting Information (Table S3). In turn, the detection of 4-oxohomoadamantan-5-one was unambiguous, based on the agreement between the spectral data obtained for the photolysed Ar matrix of **TX** and the spectrum of a genuine sample of 4-oxohomoadamantan-5-one isolated in an Ar matrix reported before.[17] In this case, all bands calculated as having an intensity above 5 km mol^{-1} were observed experimentally and at positions matching well those reported previously[17] (Table 2; Table S3, in the Supporting Information, presents the full calculated IR spectrum of this compound).

A final remark shall be made; besides the bands due to the major oxepane-2,5-dione and 4-oxohomoadamantan-5-one

Table 2. Experimentally observed bands of the major photoproducts of **TX**, and the corresponding DFT(B3LYP)/6-311++G(3df,3pd) calculated data. Experimentally observed frequency values previously reported[17] for a genuine sample of 4-oxohomoadamantan-5-one isolated in an argon matrix are also given for comparison.[a]

Oxepane-2,5-dione			4-oxohomoadamantan-5-one			
Ar matrix (this work)	Calculated		Ar matrix (this work)	Ar matrix [17]	Calculated	
ν	ν	I^{IR}	ν	ν	ν	I^{IR}
1722	1773.2	276.1	**1749/1747**	1747	1759.0	406.7
1714	1763.8	313.4	**1466**	1465	1466.9	12.0
1500	1491.9	9.3	**1466**	1465	1466.4	13.6
1447	1463.3	18.7	**1399**	1401/1395	1399.5	31.1
1438	1434.8	4.7	**1372**	1366	1370.0	9.9
1423	1412.5	8.6	**1361**	1363/1360	1361.4	8.7
1383	1393.8	7.5	**1333**	1330/1329	1327.4	6.4
1352	1349.2	2.4	**1272**	1270/1268	1263.4	46.6
1342	1341.8	3.9	**1249**	n.obs.	1246.1	5.0
1329	1321.4	7.2	**1155**	1172/1170	1161.5	145.3
1288	1273.0	166.5	**1113**	1116/1113	1109.5	32.8
n.obs.[b]	1255.3	14.4	**1087**	1086/1085	1077.2	46.7
1237	1223.6	56.0	**1044**	1047/1044	1029.6	58.0
1195	1194.7	19.2	**n.obs.**[b]	1002/998	996.0	15.1
1174	1171.4	157.0	**980**	980	972.2	16.5
1125	1144.0	14.8	**904**	904	903.7	9.3
1098	1082.1	51.7	**826**	826	811.7	1.7
n.obs.[b]	1056.0	31.9	**788**	787	781.8	6.8
n.obs.[b]	1000.2	18.8	**750**	748	741.9	5.2
980	970.3	6.5	**542**	539	535.4	5.2
961	941.3	26.0				
879	885.0	9.7				
836	843.0	14.6				
750	742.8	4.4				
589	570.4	9.9				

[a] Calculated wavenumbers (ν) in cm^{-1}, were scaled by 0.983. Infrared intensities (I^{IR}) in km mol^{-1}. n.obs., not observed. [b] Superimposed with an intense band of **TX** (see text for discussion).

photoproducts, the spectra of the photolysed matrices also exhibit the characteristic bands of CO_2 and CO, at 2344/2339/664 and 2139 cm^{-1}, respectively, testifying the occurrence of additional secondary minor reactions. However, while the CO_2 and CO bands were easy to observe since they occur in otherwise clean spectral regions, no spectral features ascribable to the putative accompanying products could be detected.

EPR study on the photolysis of TX isolated in an acetonitrile matrix

In situ electron paramagnetic resonance (EPR) spectroscopy was conducted during the photolysis of **TX** (100 mM) using 266 nm laser (2 mJ/pulse) in an acetonitrile matrix at 10–50 K (Figure 4). The X-band EPR signals were measured at a resonance frequency of 9.40 GHz. In the photolysis of **TX** at

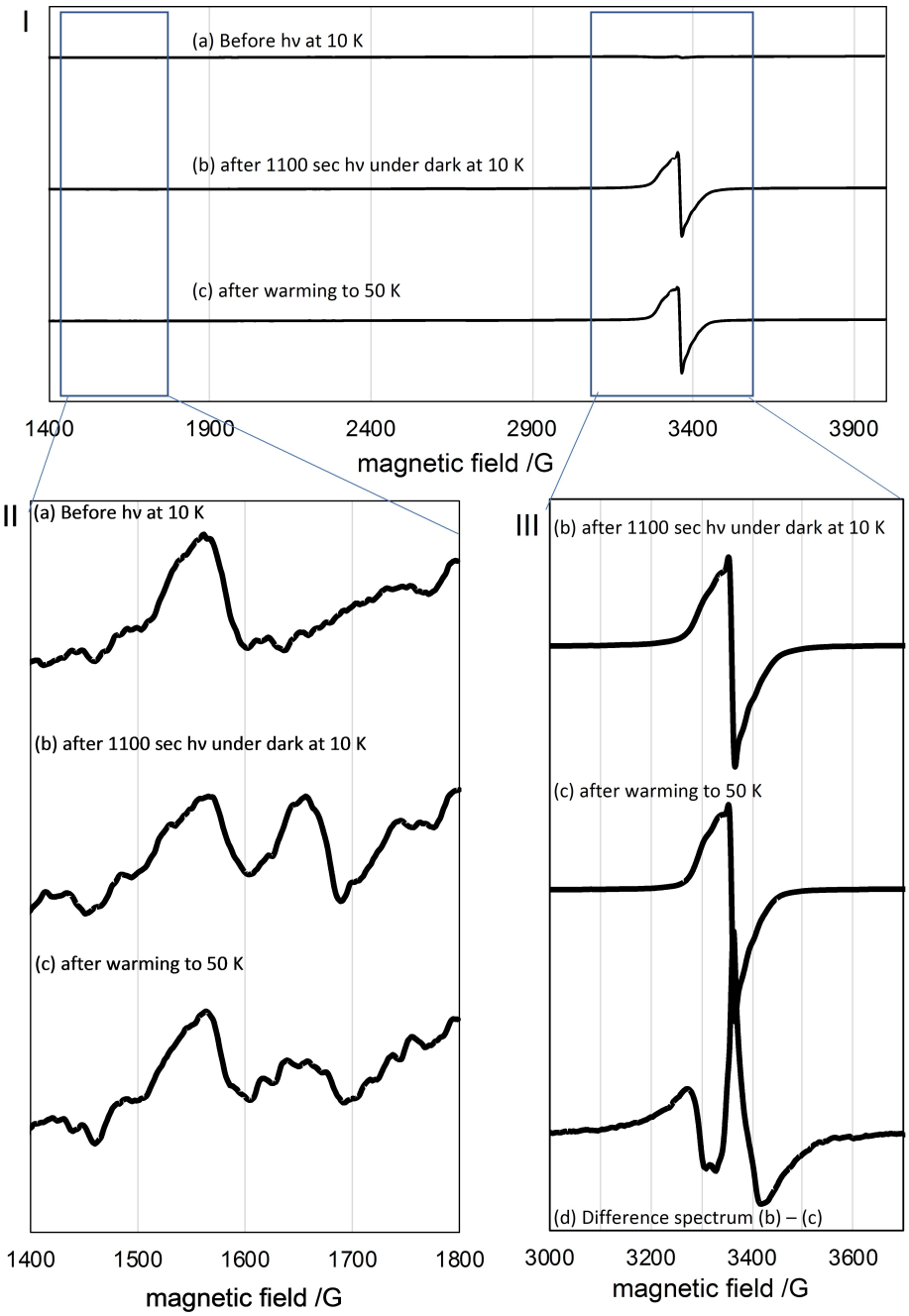

Figure 4. (I) X-band EPR spectra (9.40 GHz, 1400–4000 G) obtained from photolysis of compound TX (100 mM) in ACN-matrix, at 266 nm (2 mJ/pulse); (a) before irradiation at 10 K; (b) after irradiation for 1100 s, under dark, at 10 K (c) after warming the sample to 50 K, and subsequent recooling to 10 K (II) X-band EPR signals (9.40 GHz, 1400–1800 G) from photolysis of compound TX (100 mM) in ACN-matrix at 266 nm (2 mJ/pulse); (a) before photolysis at 10 K; (b) after 1100 s photolysis, under dark, at 10 K; (c) after warming the sample to 50 K, and subsequent recooling to 10 K; (III) X-band EPR signals (9.40 GHz, 1400–1800 G) from photolysis of compound **TX** (100 mM) in ACN-matrix at 266 nm (2 mJ/pulse) (b) after 1100 s photolysis, under dark, at 10 K; (c) after warming the sample to 50 K, and subsequent recooling to 10 K (d) difference spectrum between (b)–(c).

10 K (Figure 4b), a half-field signal at ~1650 G (triplet diradical species) was observed after 1100 sec irradiation (Figure 4IIb). To obtain information about the reactivity of paramagnetic species, the sample was warmed to 50 K and recooled to 10 K to measure the spectrum. The significant depletion of half-field signal was observed (Figure 4IIc), indicating that the diradical species is thermally unstable above the temperature of 50 K. The phenomenon was like the reactivity of diradical **3**, which was also thermally labile. In the photolysis of peroxide **1**, we could observe another diradical **2**. However, the corresponding diradical **2′** was not detected under similar photolysis conditions for **TX**. The observation can be reasonably explained by the presence of another photo-labile peroxide bond in **2′**. To analyze in more detail the structure of diradical **3′**, the allowed transition signals (3000—3600 G) were obtained by subtracting Figure 4IIIc from Figure 4IIIb (Figure 4IIId). However, the zero-field splitting parameters *D* and *E* were not determined due to the broad signals of the allowed transitions not to estimate the radical-radical distance (Figure 4d).

Crystal structure of TX

A single-crystal X-ray diffraction study was performed that enabled an unambiguous determination of the molecular conformation of **TX** in the solid state (Figure 5). The compound crystallizes in the monoclinic $P2_1/n$ (SG #14) space-group, with four (one symmetry-independent) molecules per unit cell ($Z=4$, $Z'=1$).

The tetraoxane ring of the **TX** molecule in the crystalline state was found to adopt the most stable conformation predicted by the DFT calculations on the isolated molecule, the chair conformation, with a weighted average torsion angle of 64.9(5)° and Cremer and Pople[30] puckering amplitude $Q=$ 0.6464(10) Å and angles $\theta=1.41(9)°$, $\varphi=358(3)°$ ($q_{2=}$ 0.0179(10) Å, $q_{3=}0.6462(10)$ Å, $\varphi_{2=}358(3)°$, taking O1 as pivot atom, and O1→O2 as the sense of rotation in the ring; see Figure 5 for atom numbering). The 6-membered rings of the adamantane moiety also adopt close to ideal chair conformations. The 8-membered ring of this moiety adopts the usual Boat-Boat form. The Cremer and Pople parameters of the cyclohexane ring are $q_{2=}0.1223(15)$ Å, $\varphi_{2=}354.4(7)°$, and $q_{3=}$ 0.4956(15) Å, corresponding to a puckering amplitude $Q=$ 0.5105(15) Å and angles $\theta=13.86(17)°$, $\varphi=354.4(7)°$ (taking C4 as pivot atom, and C4→C12 as the sense of rotation in the ring), showing that conformation of this ring deviates significantly from the chair ($\theta=0°$) towards the half-chair ($\theta=30°$) conformation. Bond lengths and angles are unexceptional, with average bond lengths Csp^3–Csp^3 1.528(6) Å [1.531 Å], Csp^2–Csp^2 1.501(2) Å [1.505 Å], C–O 1.426(3) Å [1.430 Å], O–O 1.470(4) Å [1.474 Å] and O=O 1.2042(19) Å [1.206 Å] (values given in brackets are corrected for molecular vibration from a fit of the anisotropic displacement ellipsoids to a rigid-body TLS model[31]).

The packing of the molecules in the crystal structure is mainly dictated by van der Walls interactions, as the molecule lacks donor groups for conventional hydrogen bonding. An inspection for potential short contacts in the crystal structure discloses only the two intramolecular short contacts C2–H2B···O1 [2.8678(14) Å] and C9–H9B···O1 [2.7738(15) Å]. The molecular packing in the crystal is shown in Figure 6.

IR spectrum of crystalline TX

The room temperature (RT) infrared spectrum of crystalline **TX** was obtained, and it is shown in Figure 7, where it is compared with that obtained for the isolated molecules of the compound in an argon matrix (15 K). As seen in the figure, the two spectra are very much alike, this being in consonance with the structural data obtained by XRD, which indicates that the intermolecular interactions in the crystal are rather weak, mostly of dispersive nature, so that the intermolecular potential experienced by the **TX** molecules in the crystal does not perturb in a significant way the intramolecular vibrational potential. The similarity of the two spectra also reflects the fact that the structure of the **TX** molecules in the **CC** conformation, found to be present under matrix isolation conditions, is approximately kept in the crystalline phase despite the observed distortion of the cyclohexanone fragment in the crystal pointed out in the previous section. Table 3

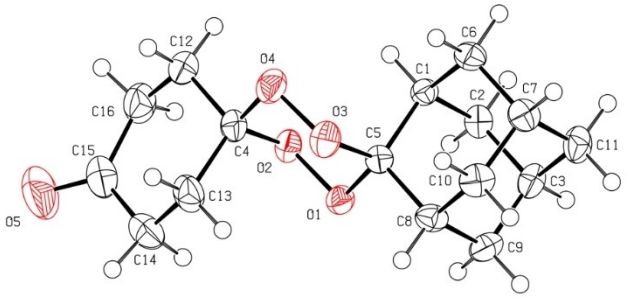

Figure 5. ORTEP plot depicting the anisotropic displacement ellipsoids drawn at the 50% probability and the atom numbering scheme of the **TX** molecule.

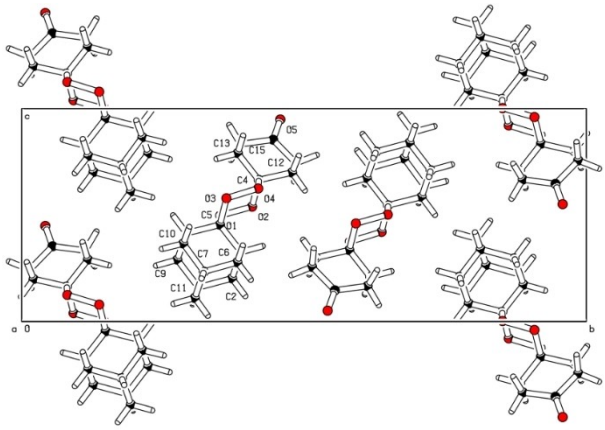

Figure 6. Projection of the crystal structure of **TX** along the monoclinic *b*-axis, showing the molecular packing.

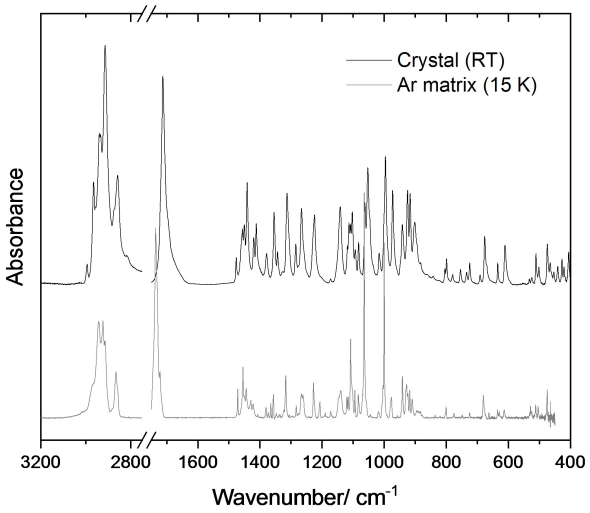

Figure 7. Infrared spectrum of the room temperature (RT) crystalline TX, compared to the infrared spectrum obtained for the matrix-isolated molecules of TX (argon matrix; 15 K).

presents the proposed band assignments, which closely follow those presented for the matrix-isolated compound (see also Table 1).

Conclusions

The work describes the synthesis, molecular and crystal structure, vibrational spectroscopy, and photochemistry of a tetraoxane with effective and broad antiparasitic activity, dispiro[cyclohexane-1,3′-[1,2,4,5]tetraoxane-6′,2′′-tricyclo[3.3.1.1^{3,7}]decan]-4-one (**TX**). a tetraoxane.

The molecular structure of **TX** was studied by matrix isolation infrared spectroscopy and quantum chemical calculations undertaken at the DFT(B3LYP)/6-311++G(3df,3pd) level of theory, with and without consideration of dispersion interactions.

Among the five conformers found on the potential energy surface of the **TX** molecule, calculations predicted two low-energy conformers, the most stable bearing both tetraoxane and cyclohexanone rings in a chair conformation (**CC**), while the second conformer in the increasing order of energy (**CTB**) bears the tetraoxane ring in the chair conformation (like in **CC**) but the cyclohexanone in a twisted-boat conformation. Consideration of dispersive interactions in the calculations was found to not change this picture, resulting only in a small additional stabilization of the more stable **CC** conformer. The experimental data indicates that, upon deposition of the compound in an argon matrix, only this latter conformer (**CC**) subsists, with the **CTB** form being converted into **CC** under the conditions used for matrix deposition.

The photochemistry of the matrix-isolated **TX** was also investigated. The experiments involved-excitation with both in situ broadband ($\lambda > 235$ nm) or narrowband (λ in the range 220–263 nm) irradiations, and the photochemical events were monitored by FTIR and EPR spectroscopies. Analysis of the infrared spectrum revealed new bands that could be ascribed to two distinct photoproducts, oxepane-2,5-dione **4** and 4-oxohomoadamantan-5-one **5**′ (Scheme 2).

In situ EPR measurements during photolysis at $\lambda = 266$ nm of **TX** deposited in an acetonitrile matrix at 10–50 K led to the detection of a half-field signal at ~1650 G (triplet diradical species), observed after 1100 sec irradiation at 10 K. Significant half-field signal depletion was observed when warming to 50 K and subsequent recooling to 10 K, indicating that the diradical species is thermally unstable above 50 K. The phenomenon resembled the thermally unstable reactivity of the diradical **3** (Scheme 2), observed from photolysis of the previously studied trioxolane **1**. However, another diradical **2** could then be observed, while under similar photolysis conditions, the corresponding diradical **2**′ for **TX** was not detected, which could be explained by the presence of another photo-labile peroxide bond in **2**′. From the FTIR and EPR results, we propose a photodegradation pathway for tetraoxane **TX** involving the initial cleavage of an O–O bond, leading to the formation of the oxygen-centered diradical **2**′, which regioselectively rearranges to a more stable (secondary carbon-centered)/(oxygen-centered) diradical species **3**′, which then reorganizes to the identified final products, **4** and **5**′.

The structure of the neat solid crystalline compound was determined by single-crystal X-ray diffraction (XRD), with the **TX** molecule adopting nearly the same conformation in the crystal as observed for the matrix-isolated compound (**CC** form, with a distorted chair-conformation of the cyclohexanone ring in the crystal). The structural XRD data also revealed that the intermolecular interactions in the **TX** crystal are weak, in keeping with the fact that the infrared spectrum of the crystalline material is significantly similar to the IR spectrum obtained for the matrix-isolated molecules of the compound.

The detailed structural, vibrational, and photochemical data here disclosed deepens the understanding of the structure and photoreactivity/photostability of antiparasitic endoperoxides based on the tetraoxane pharmacophore; thus, it is of relevance in medicinal chemistry.

Experimental Section and Computational details

Chemicals: All reagents for synthesis were purchased from commercial sources and used without further purification. Analytical thin-layer chromatography (TLC) was carried out using Merck TLC Silica gel 60F254 aluminium sheets and visualized under UV or by the appropriate stain, *p*-anisaldehyde, and potassium permanganate being the most used. Column chromatography was carried out using Sigma Aldrich technical grade silica gel (pore size 60 Å, 230–400 mesh particle size, 40–63 μm particle size).

Equipment for General Characterization of the Compounds: ^{1}H and ^{13}C nuclear magnetic resonance (NMR) spectra were recorded using a 400 MHz Bruker instrument or a 500 MHz JEOL system, equipped with a Royal HFX probe in the deuterated solvents described in each experimental procedure. The chemical shifts (δ) are described in parts per million (ppm) downfield from an internal standard of tetramethylsilane (TMS). Melting points (°C) were obtained on an SMP30 melting point apparatus and are uncor-

Table 3. Assignment of the room temperature (RT) infrared spectrum of **TX** (crystalline phase).[a]

Crystal (RT)	Approximate description	Crystal (RT)	Approximate description	Crystal (RT)	Approximate description
3026	νCH_2 as *m* chx	**1362**	wCH_2 ad	**973**	νCC chx
2994	νCH_2 as *o* chx	**13555**	wCH_2 *m*, *o* chx	**940**	νOO s
	νCH_2 as *o* chx		wCH_2 ad	**924**	νCC ad
	νCH prox ad		wCH_2 ad		γCH_2 *m* chx
	νCH_2 as *m* chx	**1343**	wCH_2 *m*, *o* chx	**916**	γCH_2 *m* chx
2966	νCH_2 as ad	**1329**	δCH ad	**902**	νCO as (chx-side); νCC chx
	νCH_2 as ad	**1325**	wCH_2 ad		νCC ad
	νCH_2 as ad	**1312**	$twCH_2$ *m*, *o* chx	**894**	γCH_2 *o* chx
	νCH_2 as ad	**1305**	$twCH_2$ ad	**886**	γCH_2 term ad
	νCH prox ad		$twCH_2$ ad	**883**	γCH_2 ad
	νCH_2 s *m* chx	**1285**	$twCH_2$ ad	**864**	νOO as
	νCH_2 s *m* chx	**1275**	δCH ad	**858**	νCC ad
2939	νCH_2 as term ad	**1266**	$twCH_2$ *m* chx; wCH_2 *o* chx	**842**	νCC ad
2934	νCH a.i.p. ad; νCH_2 s ad	**1257**	νCC ad	**799**	νCC chx
2913	νCH ad	**1249**	$twCH_2$ term ad	**804**	νCC ad
	νCH_2 s *o* chx	**1228.**	$twCH_2$ ad	**779**	νCC ad
	νCH_2 s ad	**1224**	$twCH_2$ *m*, *o* chx	**754**	γC=O
	νCH_2 s *o* chx	**1206**	νCC chx	**734**	γCH_2 *o* chx
	νCH_2 s ad	**1172**	$twCH_2$ ad	**725**	νCC chx
	νCH_2 s ad	**1142**	$\nu C_\alpha C$ chx	**691**	δCC chx
	νCH_2 s ad	**1118**	δCH ad	**676**	δCC ad
2859	νCH_2 s term ad	**1113**	δCH ad	**670**	δCC ad
1713	νC=O		δCH ad	**634**	δCC ad
1476	δCH_2 ad	**1108**	γCH_2 ad	**610**	δCC chx
1456	δCH_2 *m* chx		γCH_2 ad	**532**	δtox
	δCH_2 ad	**1103**	νCC chx	**524**	τtox
	δCH_2 ad	**1093**	γCH_2 ad		τtox
1450	δCH_2 term ad	**1082**	νCC ad	**511**	δC=O
1441	δCH_2 *m* chx	**1062**	νCC ad"; νCO s (ad-side)	**502**	δ skeletal
	δCH_2 ad	**1053**	νCC ad	**474**	δ skeletal
1420	δCH_2 *o* chx	**1046**	νCO s (chx-side)	**466**	δ skeletal
1412	δCH_2 *o* chx	**1035**	νCC ad	**453**	τ ad
1379	δCH ad	**1016**	νCC chx	**440**	τ ad
	δCH ad	**996**	νCC ad	**427**	τ ad
1362	wCH_2 ad		νCO s (ad-side)	**420**	δ skeletal
	wCH_2 *m*, *o* chx	**1000**	νCO as (ad-side); νCC ad	**406**	τ chx
	δCH ad				

[a] Wavenumbers (ν) in cm^{-1}; n.obs., ν, stretching; δ, bending; w, wagging; tw, twisting; γ, rocking; τ, torsion; ad, adamantane moiety; chx, cyclohexanone ring; tox, tetraoxane ring; *m*, *meta*; *o*, *ortho*; as, anti-symmetric; s, symmetric; prox, proximal; term, terminal; a.i.p., all-in-phase. The "approximate descriptions" follow the same order as in Table 1 and correspond entry-by-entry to the calculated frequencies presented there for the isolated molecule.

rected. High Resolution mass spectrometry (HRMS) data were recorded using the analytical service within the Centre of Marine Sciences (CCMAR, Algarve, Portugal) and was conducted on a Thermo Scientific HRMS instrument, model Orbitrap Elite, capable of MSn, n up to 10.

Synthesis: The methodology described by Amado et al.[32] was adapted for the preparation of dispiro[cyclohexane-1,3′-[1,2,4,5]tetraoxane-6′,2″-tricyclo[3.3.1.1^{3,7}]decan]-4-one (**TX**). The synthesis route starts with the peroxyacetalization of 2-adamantanone using 50% (*w/w*) aqueous hydrogen peroxide, in acetonitrile, in the presence of the silica sulfuric acid catalyst (SSA), to afford the *gem*-dihydroperoxide (DHP). Cyclocondensation of the crude DHP with 1,4-cyclohexanedione, catalysed by SSA, produced the desired 1,2,4,5-tetraoxane **TX**, which was purified through flash chromatography (EtOAc:hexane, 2.5:97.5, *v/v*). White solid (8% yield). M.p = 429.15–431.15 K. Spectral data are in accordance with the reported in the literature.[32,33] ^{1}H NMR (500 MHz, $CDCl_3$): δ 3.20 (br s, 1H), 2.72 (s, 2H), 2.48 (br d, *J* = 24.5, 4H), 2.10–1.86 (m, 9H), 1.82–1.59 (m, 6H);

$^{13}C\{^1H\}$ NMR (126 MHz, $CDCl_3$): δ 209.4, 111.1, 106.7, 37.0, 36.5, 35.7, 34.4, 33.2, 30.5, 30.2, 28.0, 27.1; HRMS (ESI$^+$, *m/z*) calcd. $C_{16}H_{22}O_5Na$ $[M+Na]^+$: 317.13594; found 317.13599. Diff: −0.16 ppm.

Argon Matrix Isolation Infrared Spectroscopy Measurements: A sample of **TX** was placed in a homemade thermoelectrically heatable mini-oven installed inside the cryostat chamber. The matrices were then prepared by co-deposition of the vapor of the compound (by sublimation) and large excess of Ar (N60, supplied by Air Liquide) onto a CsI substrate assembled at the cold-tip (15 K) of the cryostat (APD Cryogenics closed-cycle helium refrigeration system, with a DE-202 A expander). The temperature of the cold CsI window was measured directly at the sample holder by a silicon diode sensor using a digital temperature controller (Lakeshore 335) with an accuracy of 0.1 K.

The mid-IR spectra, in the 4000–400 cm^{-1} range, were obtained using a Thermo Nicolet 6700 Fourier transform IR spectrometer, equipped with a deuterated triglycine sulphate (DTGS) detector and a Ge/KBr beam splitter, with 0.5 cm^{-1} spectral resolution. To avoid interference from atmospheric H_2O and CO_2, a stream of dry, CO-filtered air was continuously purging the optical path of the spectrometer.

Broadband irradiation was carried out with UV light ($\lambda > 235$ nm) provided by a 500 W Hg(Xe) arc lamp (Newport, Oriel Instruments), with output power set to 200 W, through the outer quartz window of the cryostat and a water filter. Matrices were also irradiated with tunable UV light ($\lambda = 220$, 230, 250 and 263 nm) provided by the frequency doubled signal beam of the Spectra Physics Quanta-Ray MOPO-SL pulsed (duration 10 ns) optical parametric oscillator (FWHM ~0.2 cm^{-1}, repetition rate 10 Hz, pulse energy ~1 mJ) pumped with a pulsed Nd:YAG laser.

Acetonitrile Matrix Isolation EPR Spectroscopy Measurements: A 100 mM solution of **TX** in acetonitrile (100 μL) was degassed under high vacuum (~3.0×10^{-2} Pa) in a quartz EPR tube, which was sealed after three freeze-pump-thaw cycles under vacuum conditions. The solution was then irradiated ($\lambda = 266$ nm; 5 mJ; provided by a Nd-YAG laser Spectra Physics Indi-40) in the EPR cavity at 10 K. The X-band EPR signals were obtained at a resonance frequency of 9.40 GHz using a Bruker E500 spectrometer at 10–80 K.

X-ray Crystallography: Single-crystal X-ray diffraction (XRD) measurements were performed at room temperature on a Bruker APEX II diffractometer equipped with a 4 K CCD detector, using graphite monochromated $Mo_{K\alpha}$ ($\lambda = 0.71073$ Å) radiation. The structure was solved by the dual-space algorithm implemented in SHELXT-2018/2,[34] and refinement of the structural model was performed with full-matrix least-squares using SHELXL-2018/3.[35] All non-hydrogen atoms were refined anisotropically. Hydrogen atoms were placed at calculated idealized positions and refined as riding using SHELXL-2018/3 default values. Full details of the data collection and structure refinement procedures are provided in the Supporting Information (Crystallographic Data).

Deposition Number 2053096 (for TX) contains the supplementary crystallographic data for this paper. These data are provided free of charge by the joint Cambridge Crystallographic Data Centre and Fachinformationszentrum Karlsruhe Access Structures service.

Computational Details

The quantum chemical calculations were performed with Gaussian 16 (Revision B.01)[36] at the density functional theory level, using the B3LYP functional[37–39] and the 6–311++G(3df,3pd) basis set,[40] with and without inclusion of the Grimme's three-body term dispersion correction D3[41] and Becke-Johnson (BJ) damping.[42–45] The conformational search was undertaken using the program CREST (an abbreviation of Conformer-Rotamer Ensemble Sampling Tool),[46,47] which utilizes the GFN2-xTB (Geometries Frequencies Non-covalent interactions extended Tight Binding)[48,49] semi-empirical quantum chemical method in the conformational search, together with the iMTD-GC (iterative Meta-Dynamics – Genetic Crossing) algorithm. The found minimum energy structures were then reoptimized at the DFT level in Gaussian 16, using the "very tight" optimization criteria. Harmonic vibrational wavenumbers and IR intensities were calculated at the same level of theory and scaled by 0.983 to correct them for the neglect of anharmonicity, basis sets restraints and the effect of incomplete treatment of the electron correlation. Calculated vibrational data were used to assist the analysis of the experimental spectra. The scaling factor was determined by fitting the computed harmonic to the experimental IR wavenumbers of **TX** within the 1500–600 cm^{-1} region. The simulation of the IR spectra was done by using Lorentzian functions with a full-width at half-maximum (FWHM) of 2 cm^{-1} and centered at the calculated (scaled) wavenumbers. The vibrational analysis was helped by inspection of the animated vibrations, using Chemcraft (version 1.8).[50]

Supporting Information

Optimized geometries (Cartesian coordinates) for the 5 conformers of **TX**, full calculated vibrational data for conformers **CC** and **CTB** of **TX**, oxepane-2,5-dione and 4-oxohomoadamantan-5-one, ^1H, $^{13}C\{1H\}$, COSY, HSQC NMR data, HRMS spectra of **TX**, and X-ray crystallographic data. The CIF file containing supplementary crystallographic data was deposited at the Cambridge Crystallographic Data Centre, with reference 2053096.

Acknowledgements

The authors thank the Portuguese Science Foundation (FCT; Project PTDC/QUI-QFI/1880/2020). The Coimbra Chemistry Centre (CQC) is supported by FCT through the projects UIDB/00313/2020 and UIDP/00313/2020. The Institute of Molecular Sciences is an Associate Laboratory funded by FCT through project LA/P/0056/2020. CCMar is an Associate Laboratory funded by FCT through projects UIDB/04326/2020, UIDP/04326/2020, and LA/P/0101/2020. The Centre of Physics of the University of Coimbra (CFisUC) is supported by FCT through the projects UIDB/04564/2020 and UIDP/04564/2020. Financial support was also received from the operational programmes CRESC Algarve 2020 and COMPETE 2020 through project EMBRC.PT ALG-01-0145-FEDER-022121. P.S.M.A gratefully acknowledges FCT for Grants SFRH/BD/130407/2017 and COVID/BD/152392/2022. M.A. acknowledges financial support from JSPS KAKENHI (grants no. JP17H03022, 20K21197, 21H01921, and 22K19033), JST CREST (grant no. JPMJCR18R4), and the

Uehara Memorial Foundation JPMJCR18R4). EPR measurements were performed at the Natural Science Center for Basic Research and Development (N-BARD) of Hiroshima University.

Conflict of Interests

The authors declare no conflict of interest.

Data Availability Statement

The data that support the findings of this study are available in the supplementary material of this article.

Keywords: 1,2,4,5-tetraoxane · DFT calculations, IR and EPR spectroscopies · matrix isolation · X-ray diffraction

[1] M. Klussmann, *Eur. J. Org. Chem.* **2017**, *23*, 1–18.
[2] E. A. Ashley, M. Dhorda, R. M. Fairhurst, C. Amaratunga, P. Lim, S. Suon, S. Sreng, J. M. Anderson, S. Mao, B. Sam, et al., *N. Engl. J. Med.* **2014**, *371*, 411–423.
[3] A. M. Dondorp, P. Ringwald, *Trends Parasitol.* **2013**, *29*, 359–360.
[4] N. Kumar, S. I. Khan, B. Negi, G. Rajalakshmi, P. Kumaradhas, D. S. Rawat, *Bioorg. Med. Chem.* **2009**, *17*, 5632–8.
[5] K. Haldar, S. Bhattacharjee, I. Safeukui, *Nat. Rev. Microbiol.* **2018**, *16*, 156–170.
[6] O. O. Abiodun, R. Brun, S. Wittlin, *Malar. J.* **2013**, *12*, 43.
[7] P. M. O'Neill, R. K. Amewu, G. L. Nixon, F. B. ElGarah, M. Mungthin, J. Chadwick, A. E. Shone, L. Vivas, H. Lander, V. Barton, S. Muangnoicharoen, P. G. Bray, J. Davies, B. K. Park, S. Wittlin, R. Brun, M. Preschel, K. Zhang, S. A. Ward, *Angew. Chem. Int. Ed.* **2010**, *49*, 5693–5697.
[8] P. M. O'Neill, S. Sabbani, G. L. Nixon, M. Schnaderbeck, N. L. Roberts, E. R. Shore, C. Riley, B. Murphy, P. McGillan, S. A. Ward, J. Davies, R. K. Amewu, *Tetrahedron* **2016**, *72*, 6118–6126.
[9] C. M. Woodley, P. S. M. Amado, M. L. S. Cristiano, P. M. O'Neill, *Med. Res. Rev.* **2021**, *41*, 3062–3095.
[10] Y. Li, H.-D. Hao, Q. Zhang, Y. Wu, *Org. Lett.* **2009**, *11*, 1615–1618.
[11] J. L. Vennerstrom, S. Arbe-Barnes, R. Brun, S. A. Charman, F. C. K. Chiu, J. Chollet, Y. Dong, A. Dorn, D. Hunziker, H. Matile, K. McIntosh, M. Padmanilayam, J. Santo Tomas, C. Scheurer, B. Scorneaux, Y. Tang, H. Urwyler, S. Wittlin, W. N. Charman, *Nature* **2004**, *430*, 900–904.
[12] Y. Tang, Y. Dong, X. Wang, K. Sriraghavan, J. K. Wood, J. L. Vennerstrom, *J. Org. Chem.* **2005**, *70*, 5103–5110.
[13] S. L. Rawe, *Antimalar. Agents*, Elsevier Ltd **2020**, pp. 99–132.
[14] G. dos P Gomes, V. Vil', A. Terent'ev, I. V. Alabugin, *Chem. Sci.* **2015**, *6*, 6783–6791.
[15] E. Juaristi, G. dos P Gomes, A. O. Terent'ev, R. Notario, I. V. Alabugin, *J. Am. Chem. Soc.* **2017**, *139*, 10799–10813.
[16] I. V. Alabugin, L. Kuhn, M. G. Medvedev, N. V. Krivoshchapov, V. A. Vil', I. A. Yaremenko, P. Mehaffy, M. Yarie, A. O. Terent'ev, M. A. Zolfigol, *Chem. Soc. Rev.* **2021**, *50*, 10253–10345.
[17] E. M. Brás, L. I. L. Cabral, P. S. M. Amado, M. Abe, R. Fausto, M. L. S. Cristiano, *J. Phys. Chem. A* **2020**, *124*, 4202–4210.
[18] Y. Dong, Y. Tang, J. Chollet, H. Matile, S. Wittlin, S. A. Charman, W. N. Charman, J. S. Tomas, C. Scheurer, C. Snyder, B. Scorneaux, S. Bajpai, S. A. Alexander, X. Wang, M. Padmanilayam, S. R. Cheruku, R. Brun, J. L. Vennerstrom, *Bioorg. Med. Chem.* **2006**, *14*, 6368–6382.
[19] N. C. P. Araujo, R. Afonso, A. Bringela, M. L. Cancela, M. L. S. Cristiano, R. B. Leite, *Parasitol. Int.* **2013**, *62*, 575–582.
[20] S. Cortes, A. Albuquerque, L. I. L. Cabral, L. Lopes, L. Campino, M. L. S. Cristiano, *Antimicrob. Agents Chemother.* **2015**, *59*, 5032–5035.
[21] A. V. Karnik, M. Hasan, *Stereochem. A Three-Dimensional Insight*, Elsevier Ltd **2021**, Chapter 8.
[22] N. L. Allinger, J. Allinger, M. A. DaRooge, *J. Am. Chem. Soc.* **1964**, *86*, 4061–4067.
[23] R. J. Ouellette, J. D. Rawn, *Org. Chem. Struct. Mech. Synth.*, Academic Press, London (UK), 2nd Edition **2018**, Chapter 4.
[24] N. Kuş, A. Sharma, I. Peña, M. C. Bermúdez, C. Cabezas, J. L. Alonso, R. Fausto, *J. Chem. Phys.* **2013**, *138*, 144305.
[25] A. L. B. Brito, S. Lopes, G. O. Ildiz, R. Fausto, *Molecules* **2023**, *28*, 1673.
[26] A. Secrieru, S. Lopes, M. L. S. Cristiano, R. Fausto, *Molecules* **2021**, *26*, 4299.
[27] A. Borba, M. Albrecht, A. Gómez-Zavaglia, M. A. Suhm, R. Fausto, *J. Phys. Chem. A* **2010**, *114*, 151–161.
[28] P. M. O'Neill, L. P. D. Bishop, N. L. Searle, J. L. Maggs, S. A. Ward, P. G. Bray, R. C. Storr, B. K. Park, *Tetrahedron Lett.* **1997**, *38*, 4263–4266.
[29] J. Cazelles, A. Robert, B. Meunier, *J. Org. Chem.* **1999**, *64*, 6776–6781.
[30] D. Cremer, J. A. Pople, *J. Am. Chem. Soc.* **1975**, *97*, 1354–1358.
[31] V. Schomaker, K. N. Trueblood, *Acta Crystallogr. Sect. B* **1968**, *B24*, 63–76.
[32] P. S. M. Amado, L. M. T. Frija, J. A. S. Coelho, P. M. O'Neill, M. L. S. Cristiano, *J. Org. Chem.* **2021**, *86*, 10608–10620.
[33] F. Marti, J. Chadwick, R. K. Amewu, H. Burrell-Saward, A. Srivastava, S. A. Ward, R. Sharma, N. Berry, P. M. O'Neill, *MedChemComm* **2011**, *2*, 661–665.
[34] G. M. Sheldrick, *Acta Crystallogr. Sect. A* **2015**, *71*, 3–8.
[35] G. M. Sheldrick, *Acta Crystallogr. Sect. C* **2015**, *71*, 3–8.
[36] M. J. Frisch, G. W. Trucks, H. B. Schlegel, G. E. Scuseria, M. A. Robb, J. R. Cheeseman, G. Scalmani, V. Barone, B. Mennucci, G. A. Petersson, H. Nakatsuji, M. Caricato, X. Li, H. P. Hratchian, A. F. Izmaylov, J. Bloino, G. Zheng, J. L. Sonnenberg, M. Hada, M. Ehara, K. Toyota, R. Fukuda, J. Hasegawa, M. Ishida, T. Nakajima, Y. Honda, O. Kitao, H. Nakai, T. Vreven, J. J. A. Montgomery, J. E. Peralta, F. Ogliaro, M. Bearpark, J. J. Heyd, E. Brothers, K. N. Kudin, V. N. Staroverov, R. Kobayashi, J. Normand, K. Raghavachari, A. Rendell, J. C. Burant, S. S. Iyengar, J. Tomasi, M. Cossi, N. Rega, J. M. Millam, M. Klene, J. E. Knox, J. B. Cross, V. Bakken, C. Adamo, J. Jaramillo, R. Gomperts, R. E. Stratmann, O. Yazyev, A. J. Austin, R. Cammi, C. Pomelli, J. W. Ochterski, R. L. Martin, K. Morokuma, V. G. Zakrzewski, G. A. Voth, P. Salvador, J. J. Dannenberg, S. Dapprich, A. D. Daniels, Ö. Farkas, J. B. Foresman, J. V. Ortiz, J. Cioslowski, D. J. Fox, *Gaussian 16, Revision B.01*, Gaussian, Inc.: Wallingford CT **2016**.
[37] A. D. Becke, *Phys. Rev. A* **1988**, *38*, 3098–3100.
[38] C. Lee, W. Yang, R. G. Parr, *Phys. Rev. B* **1988**, *37*, 785–789.
[39] S. H. Vosko, L. Wilk, M. Nusair, *Can. J. Phys.* **1980**, *58*, 1200–1211.
[40] M. J. Frisch, J. A. Pople, J. S. Binkley, *J. Chem. Phys.* **1984**, *80*, 3265–3269.
[41] S. Grimme, J. Antony, S. Ehrlich, H. Krieg, *J. Chem. Phys.* **2010**, *132*, 154104.
[42] A. D. Becke, E. R. Johnson, *J. Chem. Phys.* **2005**, *123*, 154101.
[43] E. R. Johnson, A. D. Becke, *J. Chem. Phys.* **2005**, *123*, 024101.
[44] E. R. Johnson, A. D. Becke, *J. Chem. Phys.* **2006**, *124*, 174104.
[45] S. Grimme, S. Ehrlich, L. Goerigk, *J. Comput. Chem.* **2011**, *32*, 1456–1465.
[46] P. Pracht, F. Bohle, S. Grimme, *Phys. Chem. Chem. Phys.* **2020**, *22*, 7169–7192.
[47] S. Grimme, *J. Chem. Theory Comput.* **2019**, *15*, 2847–2862.
[48] C. Bannwarth, S. Ehlert, S. Grimme, *J. Chem. Theory Comput.* **2019**, *15*, 1652–1671.
[49] S. Grimme, C. Bannwarth, P. Shushkov, *J. Chem. Theory Comput.* **2017**, *13*, 1989–2009.
[50] Chemcraft – Graphical Software for Visualization of Quantum Chemistry Computations. http://www.Chemcraftprog.Com.

Manuscript received: April 26, 2023
Accepted manuscript online: June 21, 2023
Version of record online: July 24, 2023